Energy & Environmental Science

ROYAL SOCIETY OF CHEMISTRY

PAPER

View Article Online
View Journal | View Issue

Cite this: *Energy Environ. Sci.*, 2023, **16**, 5891

Charge transfer complex formation between organic interlayers drives light-soaking in large area perovskite solar cells†

Charlie Henderson, [a] Joel Luke, [a] Izabela S. Bicalho,[b] Luiza Correa,[b] Emily J. Yang,[a] Martina Rimmele, [c] Harry Demetriou,[d] Yi-Chun Chin, [a] Tianhao Lan,[a] Sandrine Heutz, [d] Nicola Gasparini, [c] Martin Heeney, [ce] Diego Bagnis[b] and Ji-Seon Kim *[a]

Received 4th August 2023,
Accepted 18th October 2023

DOI: 10.1039/d3ee02571c

rsc.li/ees

Light soaking (LS) is a well-known but poorly understood phenomenon in perovskite solar cells (PSCs) which significantly affects device efficiency and stability. LS is greatly reduced in large-area inverted PSCs when a $PC_{61}BM$ electron transport layer (ETL) is replaced with C_{60}, where the ETL is commonly in contact with a thin bathocuproine (BCP) interlayer. Herein, we identify the key molecular origins of this LS effect using a combination of surface photovoltage, ambient photoemission spectroscopy, Raman spectroscopy, integrated with density functional theory simulations. We find that BCP forms a photoinduced charge-transfer (CT) complex with both C_{60} and $PC_{61}BM$. The C_{60}/BCP complex accelerates C_{60} dimer formation, leading to a favourable cascading energetic landscape for electron extraction and reduced recombination loss. In contrast, the $PC_{61}BM$/BCP complex suppresses $PC_{61}BM$ dimer formation, meaning that $PC_{61}BM$ dimerisation is not the cause of LS. Instead, it is the slow light-induced formation of the $PC_{61}BM$/BCP CT complex itself, and the new energetic transport levels associated with it, which cause the much slower and stronger LS effect of $PC_{61}BM$ based PSCs. These findings provide key understanding of photoinduced ETL/BCP interactions and their impact on the LS effect in PSCs.

Broader context

Perovskite solar cells have seen significant advances in power conversion efficiency (PCE) over the last decade. Inverted (p–i–n) structure perovskite solar cells (PSCs) have seen recent rapid increases in their PCEs and are approaching those of the best n–i–p devices. This has largely been driven by new self-assembled monolayer hole transport materials, whilst the traditional fullerene/bathocuproine (BCP) bilayer electron transport layers have remained unaltered. Despite its widespread use in both organic and perovskite optoelectronics, the mechanism by which BCP improves the performance of devices is still unclear. Using light soaking as a probe we shed light on the critical role BCP plays in electron extraction. We find that the electron-rich pyridyl rings in BCP donate electron density onto the electron-deficient fullerene cage, forming a charge-transfer (CT) complex. The formation rate of these CT complexes is affected by the molecular structure of the fullerene used, with evaporated C_{60} forming CT complexes with BCP spontaneously whilst solution processed $PC_{61}BM$ requires a period of illumination to form CT complexes with BCP. We find evidence for new electronic states associated with these CT complexes. These new states, which lie within the band gap of BCP, enable electron transport through this wide band gap semiconductor.

[a] *Department of Physics and Centre for Processable Electronics, Imperial College London, London SW7 2AZ, UK. E-mail: ji-seon.kim@imperial.ac.uk*
[b] *Oninn, Av. José Cândido da Silveira 2000 - Horto Florestal, Belo Horizonte, MG31035-536, Brazil*
[c] *Department of Chemistry and Centre for Processable Electronics, Imperial College London, London W12 0BZ, UK*
[d] *Department of Materials and Centre for Processable Electronics, Imperial College London, London SW7 2AZ, UK*
[e] *KAUST Solar Center, Physical Science and Engineering Division, King Abdullah University of Science and Technology (KAUST), Thuwal, 23955-6900, Saudi Arabia*
† Electronic supplementary information (ESI) available. See DOI: https://doi.org/10.1039/d3ee02571c

Introduction

In the last decade, solar cells utilising metal halide perovskite photoactive layers have seen unprecedented improvements in device performance, with certified power conversion efficiencies now approaching 26%.[1] Light soaking (LS), where the performance of a photovoltaic device improves over a period of illumination, is a known but poorly understood issue in perovskite solar cells (PSCs). LS can occur at greatly differing rates, taking from a few seconds to tens of minutes to saturate.[2]

There is no single mechanism to which LS can be universally attributed, with several competing mechanisms usually contributing. Despite its complexity, LS in PSCs is largely attributed to energetic and chemical changes at the perovskite/charge transport layer (CTL) interfaces, although migration of ions through the bulk of the perovskite photoactive layer is also thought to contribute.[3–6] PSCs utilising $PC_{61}BM$ have been shown to be particularly susceptible to such LS effects.[4,6] Understanding of LS mechanisms is crucial to develop PSC technology further towards real commercial applications. It also provides the two key advantages. Firstly, if the mechanism is interfacial, it can provide information on the nature of that interface (*e.g.* trap state density), enabling the design of improved interfaces. For example, Shao *et al.* showed that by replacing $PC_{60}BM$ with PTEG-1 (a $PC_{61}BM$ analogue incorporating a glycolated side chain) in $MAPbI_{3-x}Cl_x$ based PSCs LS was almost completely eliminated, attributed to the higher dielectric constant of PTEG-1 suppressing interfacial recombination across the interface.[6] Secondly, if the device is to be used in low-light instead of 1 Sun conditions, light soaking processes will occur either much more slowly or not at all – representing a key mode of performance loss.[7] Here we investigate and identify the origins of such light soaking effects in large area PSCs utilising $PC_{61}BM$ and C_{60} electron transport layers (ETLs) capped with a thin layer of bathocuproine (BCP).

The first solid state PSCs had an n–i–p structure, with the perovskite layer formed on a metal oxide (*e.g.* TiO_2) ETL and below an organic (*e.g.* doped spiro-OMeTAD) hole transport layer (HTL).[8] Historically the performance of PSCs using the reverse, p–i–n, architecture has lagged behind that of n–i–p PSCs due to constraints on suitable charge transport materials and the difficulty of forming high quality perovskite films on organic HTLs.[9] However there has been increasing interest p–i–n PSCs due to lower the temperatures required for processing and good performance with dopant free CTLs. Recent advances in hole transport materials (HTMs) have led to p–i–n PSCs achieving PCEs in excess of 25%.[10,11] The majority of p–i–n structure PSCs utilise a bilayer electron transport layer (ETL) consisting of a thick (20 nm) fullerene ($PC_{61}BM$ or C_{60}) layer and a thin (<10 nm) BCP interlayer, where the thin BCP interlayer is placed between the fullerene and the cathode electrode (Fig. 1c).[9] BCP is also widely applied in organic photovoltaics (OPV) and organic light emitting diodes (OLED).[12,13] Despite its widespread use, the role of BCP in these devices is still unclear. BCP has a larger band gap (3.5 eV) than $PC_{61}BM$ (1.6 eV) or C_{60} (1.7 eV),[14,15] with a Type I heterojunction being formed at a BCP/fullerene interface.[16] This results in an energetic barrier to electron extraction from the fullerene lowest unoccupied molecular orbital (LUMO) to the BCP LUMO. Despite this undesirable interfacial energy level alignment, a substantial improvement in PSC performance is observed upon addition of a thin BCP interlayer between the fullerene ETL and cathode electrode.[17] This performance enhancement has been attributed to suppression of recombination at the ETL/cathode interface,[18,19] with electron transport taking place through the BCP *via* its mid-gap states formed by strong interactions between BCP and cathode metal atoms.[16,20,21] Tunnelling of electrons through the thin insulating BCP layer may also occur.[22]

We compare the effects of LS on large area 5 × 5 cm (active area: 0.5 cm^2) p–i–n PSCs fabricated with $PC_{61}BM$ or C_{60} ETLs. In this work $PC_{61}BM$ is viewed as the preferred electron transport material (ETM) due to its excellent solubility in common solvents making it compatible with roll-to-roll processing,[23] as opposed to a C_{60} ETL which is best formed by evaporation. The efficiencies of large area devices manufactured using scalable techniques (*e.g.* blade coating, slot die printing *etc.*) currently lag behind those of their lab-scale counterparts.[24] This is due to a number of complex factors including changes in perovskite crystallisation dynamics, inhomogeneity of layer thickness and morphology, and poorer quality of interfaces.[24,25] If perovskite solar cells are to reach their commercial potential these challenges must be overcome, in part through deeper understanding of the interfaces in these devices.

Herein we show that photoinduced fullerene/BCP interactions lead to the light soaking effect in printed p–i–n perovskite solar cells. We demonstrate how the specific molecular structure of the fullerene ($PC_{61}BM$ *vs.* C_{60}) determines such interactions with BCP. By applying a combination of advanced techniques including molecular vibrational Raman spectroscopy, ambient photoemission spectroscopy, and surface photovoltage, integrated with DFT simulations, we identify the molecular origins of photoinduced fullerene/BCP interactions where BCP promotes the formation of C_{60}/C_{60} dimers, whilst it suppresses the formation of $PC_{61}BM/PC_{61}BM$ dimers. We highlight the impact of these interactions on energetics and recombination loss in devices. Our work provides key insight into the photoinduced processes occurring at the organic ETL/interlayer interface, critical for the LS effect and highlights the importance of considering the chemical nature of interlayer materials when designing new device architectures.

Results and discussion

Light soaking effects in large area perovskite solar cells

Large area p–i–n type perovskite solar cells (5 × 5 cm, active area: 0.5 cm^2) were fabricated with device architectures: ITO/NiO/$MAPbI_3$/$PC_{61}BM$/BCP/Ag and ITO/NiO/$MAPbI_3$/C_{60}/BCP/Ag. All layers were deposited by blade coating, except for the C_{60}, BCP (C_{60} devices only) and Ag layers which were deposited by thermal evaporation. The blade coating procedures used are discussed in more detail by Castro-Hermosa *et al.*[26] Fig. 1e and f show the 1 Sun LS effect on the JV characteristics of both device architectures over ~90 s of soaking. Fig. 1b shows the change in the V_{OC} after 90 s of light soaking. The devices incorporating C_{60} ETLs show minimal LS effects (except for a small increase in FF by 0.02), whereas the $PC_{61}BM$ device shows significant LS resulting in a 150 mV increase in V_{OC}. There are no significant changes in device fill factor (FF) or J_{SC} (Table S1, ESI†), suggesting that the LS induced improvement in performance is caused mainly by a change in the energetic landscape within the device.[27] Fig. S1

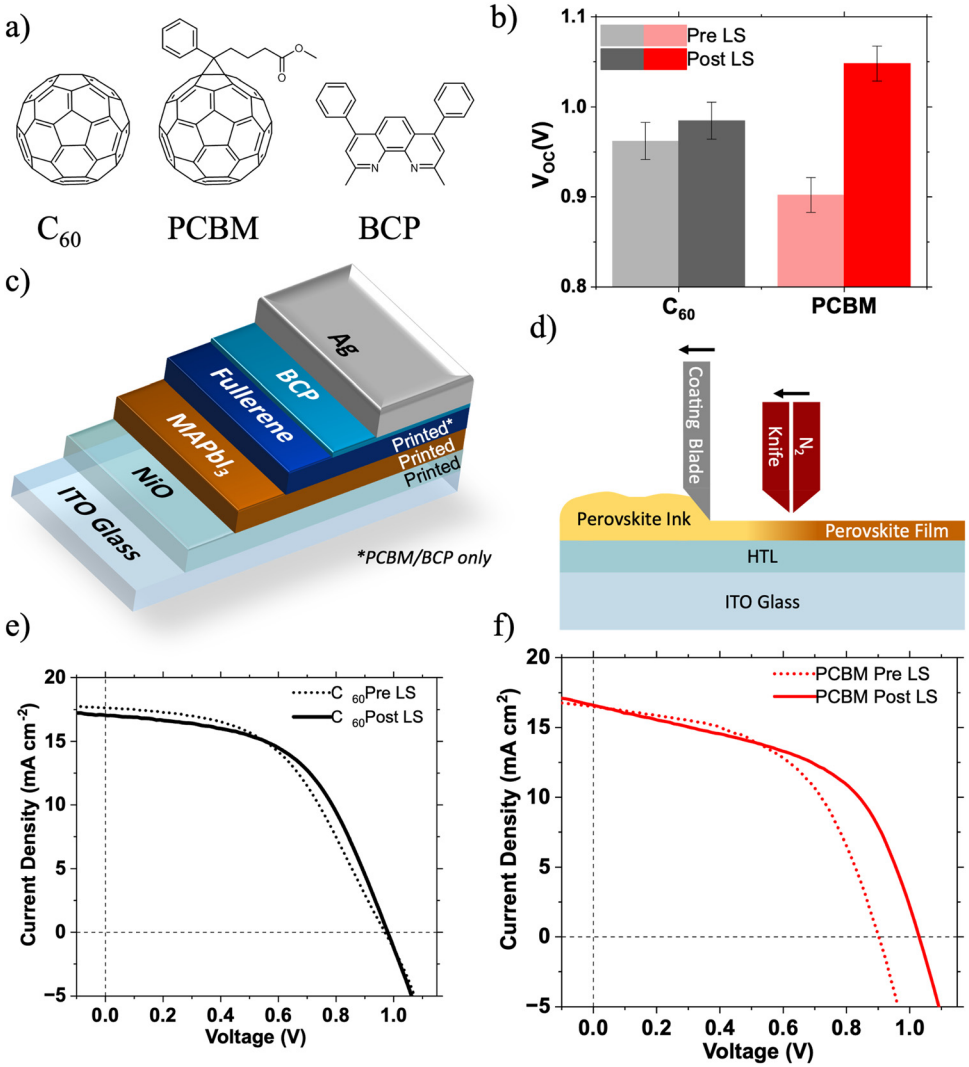

Fig. 1 (a) Chemical structures of C_{60}, $PC_{61}BM$ and BCP; (b) change in V_{OC} of $PC_{61}BM$ and C_{60} based devices between their first (S_1) and second (S_1 + 90 s) scans; (c) solar cell device structure where 'Fullerene' refers to $PC_{61}BM$ or C_{60}; (d) schematic showing the blade coating process used for the printed layers of the devices; (e) and (f) representative J–V light soaking characteristics before and after 90 s of light soaking under 1 Sun illumination for ITO/NiO/$MAPbI_3$/C_{60}/BCP/Ag and ITO/NiO/$MAPbI_3$/$PC_{61}BM$/BCP/Ag solar cells.

(ESI†) shows the change in V_{OC} of devices tested repeatedly at intervals of 12 s under 1 Sun illumination in an N_2 atmosphere. The V_{OC} of the $PC_{61}BM$ based devices takes over 72 s to stabilise, compared to less than 12 s for the C_{60} based devices. These phenomena were also observed in multiple devices utilising both $MAPbI_3$ and $Cs_xFA_{(1-x)}PbI_3$ photoactive layers (Fig. S2 and S5, ESI†).

Isolating the origin of LS *via* surface photovoltage

First, we characterise the LS effect *via* surface photovoltage (SPV). SPV uses a Kelvin probe to measure the change in surface potential of a sample upon light illumination (in this work, white light with intensity 1/5 Sun). Surface potential changes occur due to the redistribution of photo-generated charge carriers, making SPV a powerful tool to probe photogeneration, charge redistribution and loss mechanisms in partial photovoltaic device stacks.[7,27–29] We have previously demonstrated that SPV measurements can uncover the origin of light soaking in organic solar cells incorporating metal oxides ETLs.[7] Analysis of the transient behaviour of an SPV response can yield information on slow photophysical processes taking place in the device on timescales >1 s and probe charge extraction from photoactive layers (PALs) into CTLs.[27,30–32] Unlike other transient electrical measurements such as transient photovoltage (TPV) or photocurrent (TPC), SPV does not require a full device structure allowing samples to be built up layer by layer. This greater freedom in sample design allows for the contribution of each layer, and the corresponding interfaces, to loss mechanisms within the device to be isolated. As already discussed, previous work on light soaking in perovskite solar cells has focussed on the perovskite layer and its interfaces with CTLs.[4–6] To investigate which layer or interface was responsible for the LS observed, SPV was carried out on a series of samples from $MAPbI_3$ films on ITO/NiO substrates, up to near complete devices missing only the rear Ag cathode. SPV was performed

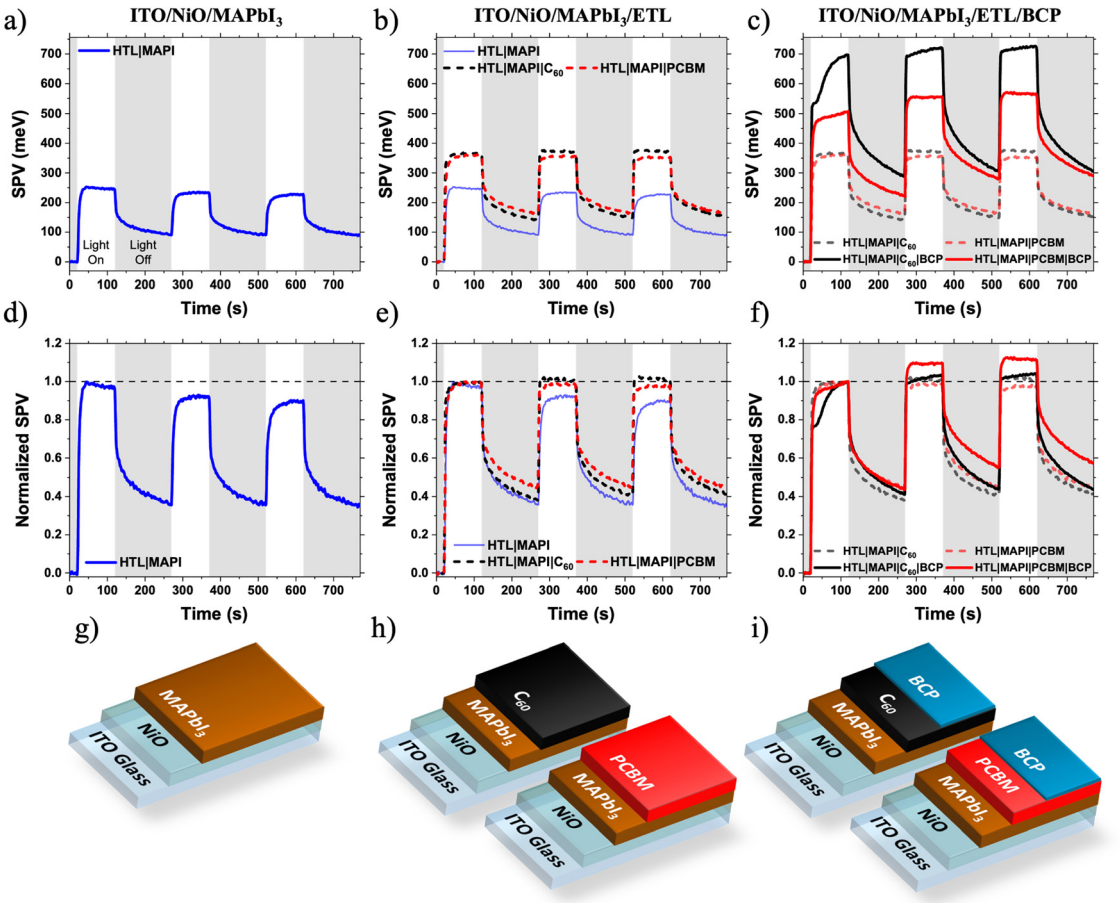

Fig. 2 (a)–(c) Surface photovoltage plots, (d)–(f) normalised surface photovoltage plots and (g)–(i) corresponding sample structure diagrams. The white regions of the SPV plots indicate periods when the sample was illuminated (white light, 1/5 Sun), grey regions indicate periods the sample was not illuminated.

using broad band white light excitation of intensity 1/5 Sun – therefore any light induced changes are expected to take place more slowly than under the 1 Sun device testing conditions.

Fig. 2 shows the SPV response of a series of partial devices based on the architecture of the full solar cells. The positive SPV response of the ITO/NiO/$MAPbI_3$ is a result of an increase in the magnitude of the contact potential difference (CPD) between the Kelvin probe and the sample. A positive SPV response is indicative of the redistribution of photogenerated charge carriers resulting in an increase of electrons at the sample surface, confirming the excellent charge selectivity of the NiO HTL. There is a slight decrease in the SPV magnitude of ITO/NiO/$MAPbI_3$ sample during the light on/off cycles measured in air (Fig. 2a and d). Interestingly, no such SPV reduction was observed in other samples where the surface of $MAPbI_3$ is covered by the ETL layer. Hence, the SPV reduction of $MAPbI_3$ sample can be attributed to an oxygen-induced photochemical effect such as superoxide generation at the $MAPbI_3$/air interface leading to changes to the surface chemistry,[33] altering photocharge generation and extraction.

There is a very little difference between the SPV responses of the ITO/NiO/$MAPbI_3$/C_{60} and ITO/NiO/$MAPbI_3$/$PC_{61}BM$ samples (Fig. 2b and e). The magnitude of SPV for both samples is similar (C_{60}: 367 meV, $PC_{61}BM$: 361 meV), consistent with the similar energetics of the two materials (Fig. S3, ESI†). Additionally, there are no significant differences in the SPV light turn-on or -off dynamics of the two samples, indicating similar slow photophysical processes such as charge trapping/de-trapping and/or chemical changes. This observation suggests that, in these devices, the perovskite/fullerene interface is not responsible for the observed LS effect in devices.

Surprisingly, upon addition of a very thin BCP layer ($PC_{61}BM/BCP_{sol\text{-}processed}$ (10 nm), $C_{60}/BCP_{evaporated}$ (5 nm)), the intensity of the SPV signal increases dramatically for both samples (C_{60}/BCP: 696 meV, $PC_{61}BM$/BCP: 506 meV at the end of the first illumination cycle). This suggests, in agreement with previous observations,[34] that BCP is active (photophysically and/or energetically) in assisting efficient charge extraction from the fullerene layer, rather than simply acting as an insulating spacer layer between the ETL and Ag electrode. The reasons for the difference in SPV response magnitude between C_{60}/BCP and $PC_{61}BM$/BCP samples are discussed later. More importantly, there is a noticeable difference in the SPV dynamics during light on/off cycles (Fig. 2c and f). When the

SPV intensities are normalised to their magnitude at the end of the first light-on cycle, a clear growth is observed in the $PC_{61}BM$/BCP signal during further cycles, which is not observed in the C_{60}/BCP signal. In the C_{60}/BCP sample's SPV response, there is a fast increase observed in the first cycle, consistent with the small change in V_{OC} at much shorter time scale in devices (Fig. S1, ESI†). However, the SPV signal of the C_{60}/BCP sample stabilises much faster than the $PC_{61}BM$/BCP, consistent with the rapid device LS shown in Fig. 1. To confirm if the differences in SPV response were due to the differing thicknesses or deposition methods of the BCP between the samples, the SPV response of an ITO/NiO/$MAPbI_3$/$PC_{61}BM$/$BCP_{evaporated}$ sample with BCP thickness of 5 nm was also measured (Fig. S4, ESI†). This sample showed similar SPV dynamics to the solution processed $PC_{61}BM$/BCP sample, confirming that the $PC_{61}BM$/BCP interface is responsible for the slow increase in SPV magnitude, matching with the slow LS effect observed in $PC_{61}BM$/BCP devices.

To confirm the generality of this observation, devices and films with the $MAPbI_3$ layer replaced with $Cs_xFA_{1-x}PbI_3$ were also fabricated. Again, the C_{60} based solar cells exhibited minimal light soaking behaviour and the $PC_{61}BM$ based solar cells exhibited strong light soaking behaviour (Fig. S5, ESI†). The same SPV experiment was performed. Although the $Cs_xFA_{1-x}PbI_3$ SPV shows much slower SPV response than $MAPbI_3$ with the signal strength not saturating even after 100 s of illumination, a similar trend of slower SPV growth in the $Cs_xFA_{1-x}PbI_3$/$PC_{61}BM$/BCP sample than in the $Cs_xFA_{1-x}PbI_3$/$PC_{61}BM$ sample being observed (Fig. S6, ESI†). In contrast, the $Cs_xFA_{1-x}PbI_3$/C_{60} and $Cs_xFA_{1-x}PbI_3$/C_{60}/BCP samples' SPV responses are much faster – similar to the SPV responses of the $MAPbI_3$ samples shown in Fig. 2. This fast SPV response can be indicative of the thermally evaporated C_{60} passivating defects at the perovskite surface, which remain un-passivated by solution deposited $PC_{61}BM$.[35] These defects also appear to contribute to light soaking, as demonstrated by the slower LS and SPV responses of the $Cs_xFA_{1-x}PbI_3$/$PC_{61}BM$ PSCs compared to the $MAPbI_3$/$PC_{61}BM$ PSCs (Fig. 1 and Fig. S5, ESI†). Further discussion and analysis of the $Cs_xFA_{1-x}PbI_3$ SPV data can be found in the ESI.† In summary, it is still clear that addition of the BCP to the $Cs_xFA_{1-x}PbI_3$/$PC_{61}BM$ sample slows the rate of SPV signal growth (Fig. S6b, ESI†), confirming that the $PC_{61}BM$/BCP interface contributes to light soaking independently of the of the PAL used.

Revealing the molecular origin of light soaking

To probe the origin of the unexpected but critical role of the fullerene/BCP interface in light soaking, C_{60} and $PC_{61}BM$ films with and without BCP were characterised in detail as a function of illumination time. Mixed component $PC_{61}BM$:BCP and C_{60}:BCP films were prepared by spin-coating from mixed $PC_{61}BM$ and BCP 1 : 1 (by weight) solutions or by co-evaporation of C_{60} and BCP. Blended films (fullerene:BCP) were chosen over bilayers (fullerene/BCP) in order to maximise the interaction between the fullerene and BCP molecules. Raman spectroscopy was employed to probe the vibrational states of the fullerene cage in both neat and blended films (Fig. 3a and b). $PC_{61}BM$ and C_{60} show characteristic Raman peaks at 1466 cm^{-1} and 1471 cm^{-1} respectively, associated with the A_g cage breathing vibrational mode.[36–39]

To simulate the light soaking in devices, films were exposed to 1 Sun conditions in an N_2 atmosphere. Following illumination, the $PC_{61}BM$ spectrum shows the growth of a side peak at 1462 cm^{-1} (Fig. 3a, red dashed line), which is assigned to the formation of fullerene dimers *via* a [2+2] cycloaddition reaction by our DFT calculations (Fig. S8, ESI†) and existing literature.[37] Upon blending the $PC_{61}BM$ with BCP the growth of a dimer side peak is also observed upon LS under 1 Sun conditions. By deconvoluting the contributions of the lower energy dimer signal and the higher energy monomer signal the relative ratios of the two species present can be quantified (see Fig. S10 for details, ESI†). In fresh samples the deconvoluted monomer : dimer ratio is 68 : 32 in the neat $PC_{61}BM$ and 77 : 23 in $PC_{61}BM$: BCP film. Upon 1 Sun illumination, the rate of growth of the dimer side peak is slowed in the $PC_{61}BM$:BCP blend film, with the final quantity of dimer being reduced by 40% in the blend compared to the neat $PC_{61}BM$ film. Illumination of films in an N_2 atmosphere under 1 Sun followed by accelerated aging under 365 nm UV light shows the suppression of an optical absorption peak at 268 nm, coupled with an increase in absorption at around 320 nm (Fig. S9, ESI†). This observation is widely reported in the literature for neat $PC_{61}BM$ and is attributed to the formation of $PC_{61}BM$ dimers.[37,40–42] These absorption changes are reduced in the $PC_{61}BM$:BCP films compared to the neat $PC_{61}BM$ film, consistent with our Raman data and with previous observations.[43] This data indicates that $PC_{61}BM$ is stabilised towards photoinduced changes (*i.e.* photodimerisation) by blending with BCP.

Photodimerisation is also known to occur between C_{60} molecules.[44,45] Much of the work on photodimerisation of $PC_{61}BM$ has been driven by interest in its use as the acceptor phase in OPVs. However, due to C_{60}'s low solubility it has seen more limited use in OPV devices, and consequently literature on its photostability in photovoltaic devices is very limited. Fig. 3b shows the evolution of Raman spectra of evaporated C_{60} and co-evaporated C_{60}:BCP blend films during following 1 Sun illumination in an N_2 atmosphere. In the C_{60} Raman spectrum the growth of a low energy shoulder peak at 1466 cm^{-1} (red dashed line) is also observed upon illumination. This energy down-shift in the A_g peak is again associated with the formation of C_{60}/C_{60} dimers (Fig. S7, ESI†).[44,46] Oppositely to $PC_{61}BM$, the growth of the dimer side peak is accelerated in the C_{60}:BCP blend film as compared to the neat film (Fig. 3d). This acceleration occurs over short time scales, with the changes in the C_{60}:BCP blend film spectra saturating at 60% dimer to monomer ratio after 24 h of light soaking. In contrast, in the neat C_{60} film the changes continue, although at a slower rate, for the full 96 h of light soaking without saturating and exceeding the percentage of dimer formed in the blend films. Additionally, a third peak at 1461 cm^{-1} (blue dashed line) is evident in the neat film, which is not observed in the C_{60}:BCP blend. This peak at much lower energy is attributed to the formation of trimers (Fig. S8, ESI†).[47] Therefore, in contrast to

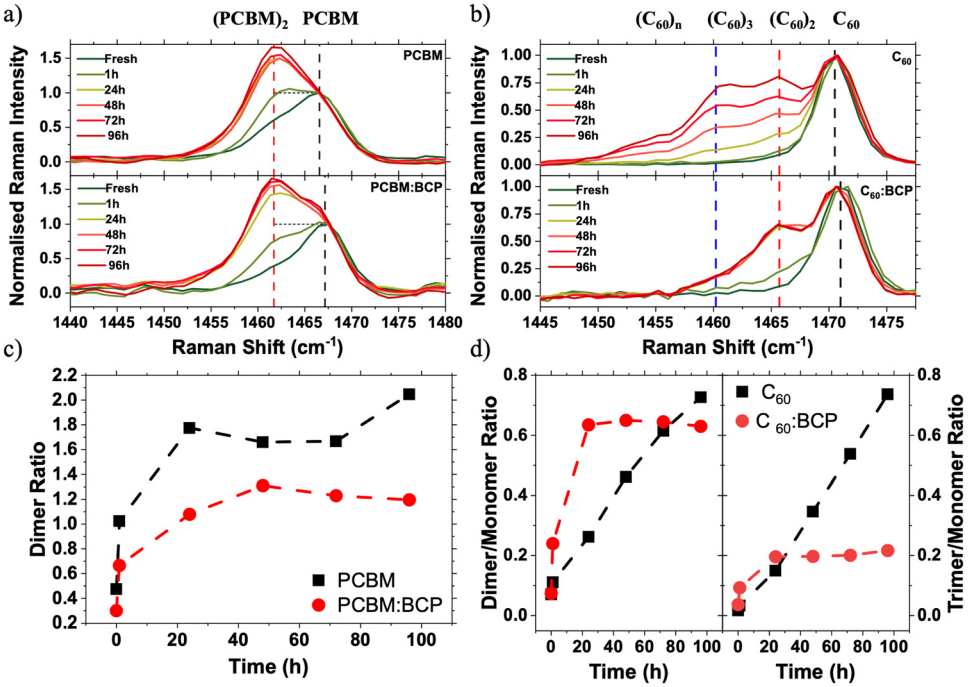

Fig. 3 Raman spectra using 785 nm excitation of neat and blended fullerene films following 1 Sun illumination under N_2. (a) Normalised Raman spectra of $PC_{61}BM$ (top) and $PC_{61}BM$:BCP (bottom) films over 96 hours of 1 Sun illumination, (b) normalised Raman spectra of C_{60} (top) and C_{60}:BCP (bottom) films over 96 hours of 1 Sun illumination. Raman spectra are normalised to the intensity of the higher energy, monomer peak. (c) Evolution of the dimer/monomer peak area ratio (*i.e.* a value of 1 indicates that monomer and dimer signals are of equal strength) for $PC_{61}BM$ (black) and $PC_{61}BM$:BCP (red), (d) evolution of the dimer/monomer (left) and trimer/monomer peak area ratios for C_{60} (black) and C_{60}:BCP (red).

$PC_{61}BM$, BCP promotes the formation of C_{60} dimers but suppresses the formation of longer oligomers. At short illumination timescales (~1 h) little change is observed in the neat C_{60} film absorption – even after additional accelerated aging under a 365 nm UV light (Fig. S9, ESI†). In contrast, the C_{60}:BCP blend film shows a significant decrease in the absorption maximum at 265 nm upon aging. This supports the interpretation of the Raman spectra and confirms that the photodimerisation rate of C_{60} is increased upon blending with BCP.

Increased Raman intensity in the 1450–1455 cm^{-1} region of the neat C_{60} spectra (Fig. 3b) suggests that longer chain oligomers or photopolymers are also formed under continuous illumination. This side peak growth can be most clearly seen in the increase of the unfitted area of Fig. S10c (ESI†). This is confirmed by comparison of the solubility of photoaged C_{60} and C_{60}:BCP films in toluene. As shown in Fig. S14 (ESI†) neat C_{60} films exhibit very poor solubility, whereas the photoaged C_{60}:BCP films dissolve readily, leaving no observable residue[44,45] This observation confirms that oligomers are formed in the neat C_{60} films upon photoaging, compared to mainly dimers (expected to be much more soluble) in the C_{60}:BCP films.

To further confirm the presence of dimers, high-pressure liquid chromatography (HPLC) measurements were performed with solutions prepared by dissolving fresh and photoaged films in toluene (Fig. S11, ESI†). The intensity of absorption at the retention time of the dimers is suppressed in the $PC_{61}BM$:BCP blend film. By comparing the integrated areas of the monomer and dimer absorption peaks, the dimer:monomer can be quantified. Following aging for 24 h the dimer ratio is reduced by 7% in the blend compared to the neat sample, increasing to a 19% reduction after 96 h (Fig. S12, ESI†). This data supports the analysis of the Raman and absorption spectra, that BCP stabilises $PC_{61}BM$ by reducing the rate at which photodimerisation occurs. Further discussion of the HPLC analyses, including on C_{60} films, can be found in the ESI.†

To explain these observations, we first discuss the important role of BCP in stabilising $PC_{61}BM$ against photoinduced changes. This brings us to one of BCP's key properties, its chelating behaviour. BCP is known to interact strongly with metal atoms and ions as a bidentate ligand *via* the two nitrogen lone pairs on its pyridyl rings, enabling gap state formation.[15,48,49] Additionally, BCP is also thought to donate electron density to electron deficient organic molecules such as $PC_{61}BM$.[43,50] For example, Hang *et al.* observed that a BCP analogue, Bphen, stabilises $PC_{61}BM$ against light induced degradation when applied as an interlayer at the SnO_2/perovskite interface in an n–i–p PSC.[43] The stabilisation of $PC_{61}BM$ by Bphen is attributed to donation of lone pair electron density from the pyridyl group to the fullerene cage, forming a charge transfer (CT) complex. As BCP differs from Bphen only in the presence of a methyl group at the *ortho* position of the pyridine ring, it is reasonable to conclude that the mechanism of stabilisation (*i.e.* charge-transfer (CT) complex formation) is similar in both systems. We observe a small (~1 cm^{-1}) upshift in both the $PC_{61}BM$ and C_{60} Raman peaks upon blending with BCP (Fig. 4a). This shift has previously been assigned to the BPhen/BCP

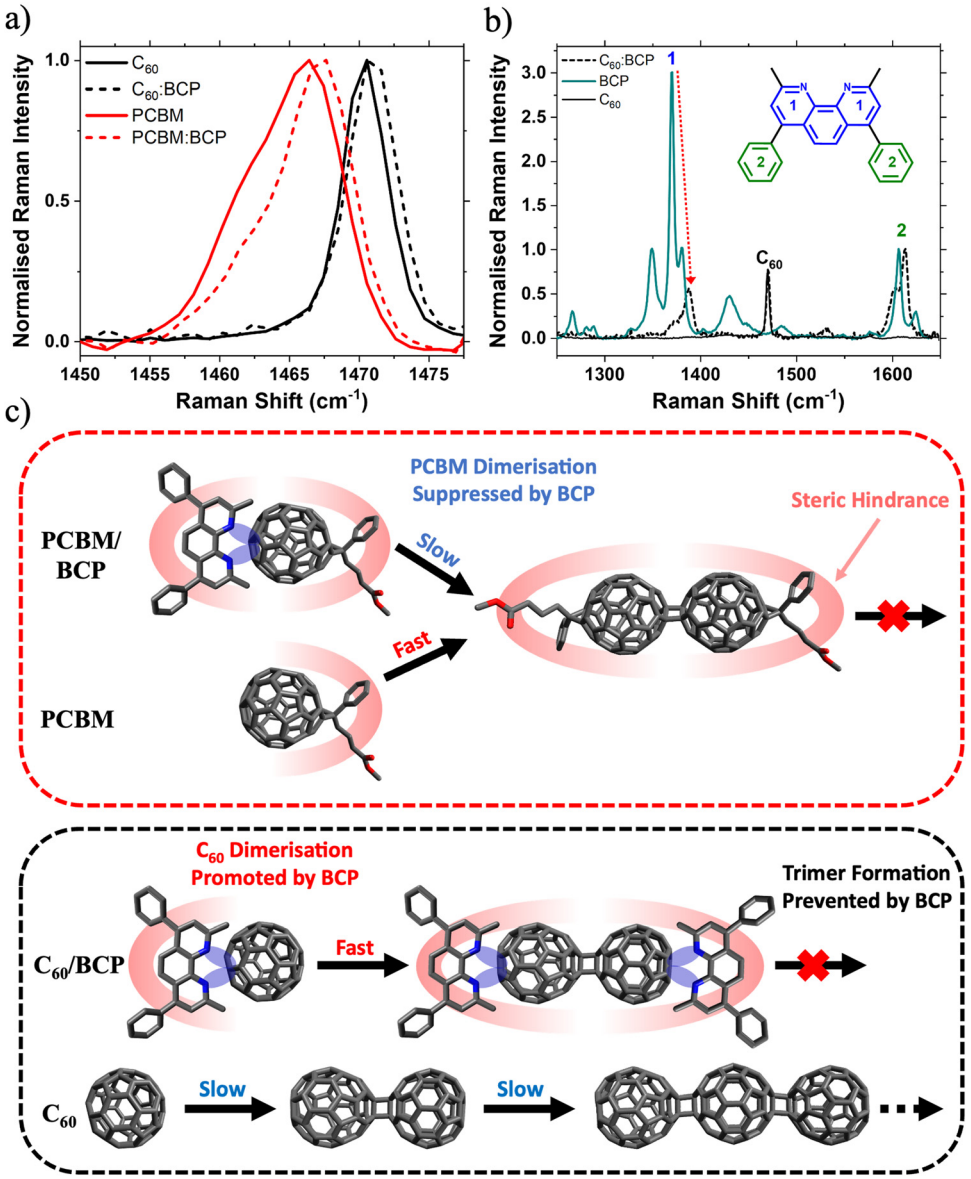

Fig. 4 Molecular origin of light soaking effect. (a) Raman spectra of C_{60} (black) and $PC_{61}BM$ (red) films and corresponding BCP blend films (dashed); (b) normalised Raman spectra of fresh C_{60}:BCP (black, dashed), BCP (blue) and C_{60} (black) films (normalisation to peak 2); (c) illustrative diagram outlining the proposed mechanism by which BCP increases the rate of C_{60} dimerisation but reduces the rate of $PC_{61}BM$ dimerisation.

CT complex with fullerenes, with increased electron density on the cage resulting in an increased effective force constant of the vibrational mode.[43,50,51] Further evidence for this interaction is given by the Raman spectra shown in Fig. 4b. BCP has characteristic Raman peaks at 1371 cm^{-1} (peak 1, intra pyridine ring C–C stretch) and 1607 cm^{-1} (peak 2, phenyl intra ring C–C stretch) respectively (Fig. S15 and Table S2, ESI†). Upon blending with C_{60} there is a dramatic reduction in the Raman intensity of the pyridine peak relative to the phenyl peak. This reduction in relative Raman activity implies that electron density is being donated from the pyridyl rings in BCP onto the C_{60}, confirming BCP/C_{60} CT complex formation. Electrostatic potential (ESP) maps of C_{60} and BCP calculated for different intermolecular spacings visualises such donation of electron density from the BCP pyridyl groups onto the C_{60} cage when two molecules are in close proximity (Fig. S16, ESI†). Calculated Raman spectra of C_{60}, BCP and the C_{60}/BCP CT complex shown in Fig. S16 (ESI†) are given in Fig. S17 (ESI†). The simulated Raman spectra match the experimental spectra closely, supporting the conclusion that CT complex formation between fullerene and BCP is confirmed the presented Raman data.

Based on our observations, we believe the rate of photodimerisation is affected differently for the two different fullerene:BCP CT complexes. In the case of $PC_{61}BM$, blending with BCP suppresses the formation of fullerene/fullerene dimers. Whereas upon blending C_{60} with BCP, dimerisation is accelerated while the formation of trimers and other oligomers is suppressed. This can be understood with reference to the molecular structures of the two fullerenes. As discussed, the

lone pairs on the BCP nitrogen groups donate electron density onto the electron deficient fullerene cage, forming a CT complex. This increased electron density may promote the formation of fullerene/fullerene dimers *via* a [2+2] cycloaddition mechanism. This explains the observation of increased dimerisation rates in the C_{60}:BCP films, compared to the neat C_{60}. Once a $(C_{60})_2$ dimer has formed, BCP is expected to preferentially arrange itself (due to steric interactions) at either end of the dimer as shown in Fig. 4c, effectively capping the molecule, and preventing longer oligomer formation. Furthermore, we expect that the dimerisation is likely to occur at the side of the fullerene furthest from the BCP for steric reasons. Similarly further reactions of the dimer to afford trimers or oligomers will be supressed because of the steric blocking effect of the BCP group. In contrast, the rate of dimer formation is lower in neat C_{60} (due to lack of electron density donation from BCP) but the formation of trimers and higher-order oligomers is no longer sterically hindered and proceeds uninterrupted. In contrast, due to the steric impact of the bulky solubilising side group on $PC_{61}BM$ the BCP can be expected to arrange itself trans to this group, sterically hindering the $PC_{61}BM$ dimerisation reaction and reducing its rate. Whereas in the neat $PC_{61}BM$ film the side group only sterically hinders the cycloaddition reaction once a dimer has formed, preventing the formation of trimers. This is supported by the work of Distler *et al.*, which showed that by replacing $PC_{61}BM$ with bis-$PC_{61}BM$ (a bis-subsituted analogue of $PC_{61}BM$) fullerene/fullerene dimerisation was suppressed by steric hindrance.[40] In this case we have only considered the trans isomer of the $PC_{61}BM$ dimer, however with other isomers (such as those reported by Pont *et al.*)[52] the effect of BCP is expected to be similar.

The photochemical processes described above are expected to occur at the fullerene/BCP interfaces in the devices. To correlate these processes to the device light soaking effect, we undertook further work to understand their effect on the energetic landscape and device physics within the PSCs. Using DFT simulations we first calculated the effect of fullerene dimerisation on the energies of the frontier molecular orbitals. Upon dimerisation the simulated HOMO levels raise by 0.21 eV and 0.13 eV for C_{60} and $PC_{61}BM$ respectively, with a corresponding deepening of the LUMO levels (Fig. S19, ESI†). Additionally, a further HOMO level shallowing of 0.06 eV is found upon conversion of a C_{60} dimer into a trimer. These changes in HOMO/LUMO levels lead to the narrowing of fullerene band gaps upon dimerisation, which are in good agreement with the absorption data (Fig. S9, ESI†). The deeper LUMO levels in dimers will lead to barrierless electron transport from fullerene monomers to dimers. Our observations above show that BCP will accelerate C_{60} dimer formation at the C_{60}/BCP interface upon illumination. Therefore, this will result in a favourable cascading energetic landscape for efficient electron transport towards the C_{60}/BCP interface, caused by a higher concentration of dimers at this interface. The C_{60}/perovskite interface is known to be a key site of energetic loss due to recombination at C_{60} trap states.[53] The cascading electron transport mechanism will reduce the accumulation of electrons in traps states at the perovskite/C_{60} interface and hence interfacial recombination at this interface. This is consistent with the rapid rise in SPV and V_{OC} observed upon initial illumination. In contrast, in the $PC_{61}BM$/BCP system, dimerisation at this interface is suppressed, so cannot gain the cascading energetic benefit as photodimer concentration will be higher in the $PC_{61}BM$ bulk. This leads us to conclude that $PC_{61}BM$ dimerisation cannot be the cause of slow light soaking observed in devices.

Next, we discuss the impact of fullerene/BCP CT complex formation on device energetic landscape. We find evidence for new electronic states associated with fullerene/BCP CT complexes in the ambient photoemission spectra (APS) in Fig. 5a and b. A shallowing of the measured HOMO levels by 110 meV for both C_{60} and $PC_{61}BM$ is observed upon blending with BCP. The APS response of neat BCP occurs at deeper energies than the neat fullerene films, so the HOMO level shallowing of C_{60} and $PC_{61}BM$ cannot be attributed to contributions from BCP's molecular orbitals. Therefore in this case we interpret this HOMO shift to lower energies as further evidence for the formation of fullerene/BCP CT complexes, similar to those reported for Ag/BCP.[16,21] Whilst APS probes the HOMO energy level, studies on BCP/metal complexes have shown concurrent HOMO shallowing and LUMO deepening upon complex formation.[15,20] This leads us to conclude that fullerene/BCP CT complexes will also possess LUMO levels deeper than neat BCP. Both $PC_{61}BM$:BCP and C_{60}:BCP films exhibit further shallowing in measured HOMO level upon light soaking for 10 minutes under 1 Sun conditions in N_2, whilst the neat films show smaller changes (Fig. 5a and b insets). In the C_{60}:BCP film the C_{60} HOMO shallows by 55 meV whilst in the $PC_{61}BM$:BCP film the $PC_{61}BM$ HOMO level shifts by 170 meV, suggesting more significant electron density transfer from BCP to $PC_{61}BM$ during LS, highlighting stronger photo-induced CT complex formation for $PC_{61}BM$ compared to C_{60}. By integrating the area below the HOMO edge of the APS spectra of both $PC_{61}BM$:BCP and C_{60}:BCP films before and after LS, the impact of CT complex formation on trap state density is assessed (Fig. S20, ESI†).[54–56] A 30% increase in the tail state area of the PCBM:BCP spectrum is observed upon LS, this is compared to a 9% decrease in the tail state area of the C_{60}:BCP spectrum. This may explain the reduced SPV magnitude of the PCBM/BCP partial device sample compared to the C_{60}/BCP sample (Fig. 2c), with the shallow PCBM/BCP gap states acting as shallow trap sites. This however does not seem to have large impact on final device performance.

Overall, the APS data suggests that the C_{60}/BCP CT complex is predominantly formed spontaneously upon BCP deposition and LS moderately improves the interfacial properties by slightly reducing trap state density. In contrast, for $PC_{61}BM$/BCP, only a modest amount of CT complex is formed spontaneously but this is significantly enhanced by light soaking, highlighting the sensitivity of $PC_{61}BM$/BCP CT complex formation towards light. Additionally, formation of the CT complex in $PC_{61}BM$:BCP during LS is associated with the formation of new energetic states and is strongly coupled with a large increase in the sub-gap trap state, suggesting a

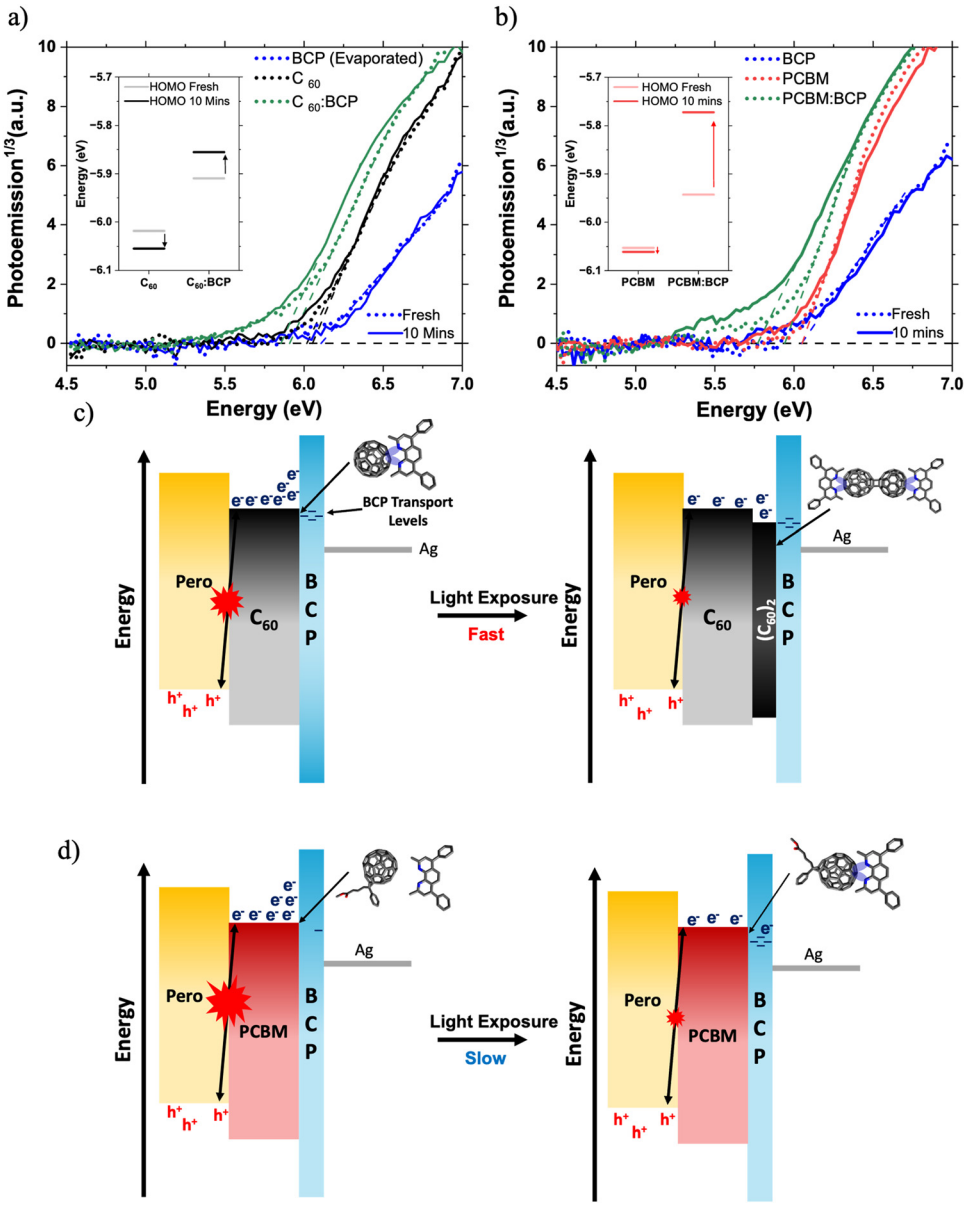

Fig. 5 The effect of light soaking on energetics at the fullerene:BCP interface. APS spectra of (a) C_{60} and (b) $PC_{61}BM$ films with and without BCP before and after 10 minutes exposure to 1 Sun conditions under N_2. Inset charts in (a) and (b) show the fitted HOMO levels before and after 10 min LS. Diagrams of proposed energetic changes in (c) C_{60} and (d) $PC_{61}BM$ based PSCs under light soaking.

significant increase in energetic disorder at the $PC_{61}BM$/BCP interface.[54,57,58] Therefore, we propose that the slow formation of these $PC_{61}BM$/BCP CT complexes under illumination is the main cause of the slow LS effect observed in the $PC_{61}BM$ containing PSCs.

Conclusions

In conclusion, we have isolated a light soaking effect in large area perovskite solar cells to the fullerene/BCP interface using SPV. This effect is independent of the perovskite photoactive layer used. We have shown that the molecular structure of the fullerene used ($PC_{61}BM$ *vs.* C_{60}) causes dramatic differences to the rate of the fullerene/fullerene dimerisation in the presence of BCP. We have linked this behaviour to LS in devices by considering the energetic effects of dimerisation and investigation of the formation of CT complex states at the fullerene/BCP interface. We find that a thin layer of $(C_{60})_2$ photodimers is formed rapidly under illumination at the interface between C_{60} and BCP which aids charge extraction to the BCP – moderately reducing recombination loss across the perovskite/C_{60} interface and leading to a small, fast increase in the device V_{OC} upon LS. In contrast, in the $PC_{61}BM$ devices LS cannot be attributed to dimer formation at the $PC_{61}BM$/BCP interface due to suppression of $PC_{61}BM$ dimerisation by BCP. Instead, we find that new

energetic states associated with light induced $PC_{61}BM$/BCP CT complex formation are essential for efficient charge transport from $PC_{61}BM$ to BCP. These BCP CT complexes predominantly form spontaneously with C_{60} but not with $PC_{61}BM$, perhaps due to the same steric effects which affect dimerisation rate. This light induced CT complex formation is evidenced by the shallowing of the measured HOMO level in the $PC_{61}BM$:BCP film upon LS. Therefore, we propose that the slow formation of $PC_{61}BM$/BCP CT complexes under illumination is the cause of the slow LS effect observed in the PSCs.

This study provides important insight into the role of the widely used fullerene/BCP electron transport system in perovskite solar cells and demonstrates that the optimisation of non-perovskite interfaces in devices is critical for further development of PSCs. As increasing effort is being put into using non-fullerene ETMs (with greater opportunity for chemical, and therefore energetic, modification) in p–i–n PSCs, the role of BCP in charge extraction will come under greater scrutiny because the majority of reported fullerene-free p–i–n PSCs still use BCP (or another interlayer) between the ETL and cathode.[59] Therefore, the design of new ETMs must take the role of BCP in devices into account.

Methods

Large-area perovskite solar cell and sample fabrication

Perovskite devices and samples were fabricated in a cleanroom in air at relative humidity in the range 30–50% using an Erichsen 510 blade coater. 50 mm × 50 mm pre-patterned glass/ITO substrates (10 Ω sq^{-1}, Thin Film Devices Inc.) were cleaned in an ultrasonic bath sequentially in aqueous detergent, de-ionised water, acetone and finally isopropanol. The substrates were dried under N_2 flow and treated by UV/O_3 (NovaScan PSD 4) for 15 minutes. After substrate cleaning, the NiO_x solution (nanoparticle solution with initial concentration of 2.5% and diluted in 1 : 5 in ethanol) was immediately blade coated using a gap of 575 μm and speed of 5 mm s^{-1}; the resulting film was annealed under an IR lamp for 2 min and after in UVO_3 for 2.5 min. The perovskite precursor ink was formed from $Pb(C_2H_3O_2)_2$, $PbCl_2$ and CH_3NH_3I with a molar ratio of 0.8 : 0.2 : 2.9 in DMF. Perovskite films were deposited by blade coating with a gap of 100 μm and speed of 10 mm s^{-1} at 43 °C, and the resulting wet film was dried with a nitrogen flow by a custom N_2 knife developed by Oninn. Samples were then transferred to a hot plate for annealing at 100 °C for 30 min. $Cs_xFA_{1-x}PbI_3$ perovskite films were fabricated using the method described above for $MAPbI_3$, with the precursor solution containing CsI, FAI and PbI_2 in a 0.17 : 0.83 : 1 molar ratio in DMF, to give a final composition of $Cs_{0.18}FA_{0.83}PbI_3$. PCBM (Nano-C, 99.82%) solutions (20 mg mL^{-1}, *o*-xylene) was deposited by blade coating with a speed of 10 mm s^{-1} and a gap of 125 μm. C_{60} (Nano-C, 99.88%) was deposited by vacuum evaporation (20 nm, 0.2 Å s^{-1}, pressure $<5 \times 10^{-6}$ mbar). BCP (TCI, >95%) was deposited from solution (isopropanol, 0.5 mg mL^{-1}) by blade coating with a gap of 100 μm at 5 mm s^{-1} for PCBM devices or by vacuum evaporation (5 nm, 0.2 Å s^{-1}, pressure $<5 \times 10^{-6}$ mbar) for C_{60} devices. Silver back electrodes were deposited by vacuum evaporation at pressures $<5 \times 10^{-6}$ mbar using a shadow mask to define eight cells with an active area of 0.5 cm^2 each.

Large area devices of size 5 × 5 cm, with 0.5 cm^2 pixels allow for 8 cells to be formed on each substrate. This has two key advantages: firstly, this enables more statistical data to be generated per substrate. The second, more important, aspect is to enable the uniformity of the coating to be understood. This allows for the stack and deposition methods to be validated, with the vision of having sufficient quality for the construction of large area modules.

Partial device stacks used for energetic characterisation were fabricated according to the steps described above, without the deposition of subsequent layers as required by the final sample structure.

Fullerene and fullerene:BCP blend films were deposited on quartz (for absorption and Raman) or ITO glass (for APS and Kelvin probe). PCBM and 50 : 50 (wt) PCBM : BCP blend films were deposited from solution (chlorobenzene, 15 mg mL^{-1}) by spin coating. C_{60} and 50 : 50 (thickness) C_{60} : BCP blend films were deposited by (co-)evaporation in a Kurt J. Lesker SPECTROS 100 system with a base pressure 10^{-7} mbar. Quartz crystal microbalances were used to precisely control the deposition rates and thickness of thin films. Films of thickness 200 nm (for Raman) and 100 nm (for APS and absorption spectra) were grown at a total deposition rate of 0.5 Å s^{-1}, from a single source, or two simultaneously in the case of blend films.

Photovoltaic characterisation

Current–voltage (*J*–*V*) characteristics of PSCs were collected under 1 Sun (AM 1.5G) illumination in N_2. No pre-biasing or light soaking was performed on the devices prior to testing. Pixels (0.5 cm^2, ×8 per device) were scanned sequentially with a step of 0.01 V and a scan rate of 0.4 V s^{-1}.

Energetic measurements and surface photovoltage (SPV)

Ambient photoemission spectroscopy and (APS) and SPV and dark work function (DWF) measurements were performed using a KP Technology APS04 system. DWF measurements were performed first, followed by SPV and finally APS; this was done to reduce the effect of any UV light induced degradation processes on other measurements. DWF and SPV measurement utilised a Kelvin probe (∅: 2 mm, Au) fitted with an off-null system,[60] calibrated using the contact potential difference (CPD) and APS response of a freshly cleaned Ag reference. SPV was performed using cycled broad band (800–400 nm) white light illumination of intensity 1/5 Sun from a quartz tungsten lamp, with simultaneous CPD measurement. SPV and DWF data was collected with measurement rate of 0.8 Hz. APS spectra were collected using a UV lamp fitted with a monochromator, with photon energies incident on the sample being varied from 4.5 to 6.8 eV. Photogenerated electrons were collected using the Kelvin probe tip biased at 10 V.[61] HOMO

levels were fitted using the linear region of the cube root of the photoemission (PE) generated current.

Raman spectroscopy

Raman spectra were collected using a Renishaw inVia Raman microscope in backscattering mode, with the sample located within a Linkam stage under continuous flowing N_2. A 785 nm diode laser, defocused by 25% to reduce sample degradation, performed the excitation. Raman spectra were collected from a minimum of 21 different sites on each sample, with the mean of these spectra being reported. No spectral changes were observed following exposures of the same sample site to the 785 nm laser for any film, ruling out laser induced degradation as a cause for our observations. Spectrometer calibration was performed using an Si reference and the PL background was subtracted using a polynomial fit. To aid visual interpretation, Raman spectra of PCBM and PCBM:BCP films were smoothed using a Savitzky–Golay filter with a window length of 6.

Simulations

Density functional theory (DFT) simulations were carried out on the Imperial College High Performance Computing service using Gaussian16 and results were visualised using GaussView 6.0.17. Simulations were performed on single molecules in the gas phase at the B3LYP (hybrid) level of theory using the 6-311G(d,p) basis set. Molecular structures were optimised to their minimum energies before Raman vibrational modes were calculated. To compare with experimental Raman spectra, a scaling factor of 0.97 was applied to the simulated Raman frequencies.[62] ESP maps were performed as single point calculations (*i.e.* molecular geometry was optimised for isolated molecules, with the ESP of C_{60}/BCP pairs being calculated without further geometry optimisation).

High performance liquid chromatography

High performance liquid chromatography (HPLC) was performed on an Agilent 1100 apparatus consisting of an G1322A degasser, G1311A quaternary pump, G1313A ALS, G1315B diode array detector (Agilent, USA) with an analytical COSMOSIL BUCKYPREP column (4.6 mm × 250 mm) and mobile phase toluene with a flow rate of 1.5 mL min^{-1}. Films were dissolved off substrates in toluene and filtered through a 0.2 μm PTFE syringe filter and 20 μL injected into the system. The diode array detector was set to two wavelengths, 290 nm and 340 nm.

Author contributions

C. H. conceived the study, performed APS, Kelvin probe, SPV and Raman measurements, performed DFT calculations, analysed data and prepared the first draft of the manuscript. J. L. prepared neat and blend $PC_{61}BM$ and $PC_{61}BM$:BCP films, assisted with experimental design, data analysis, and the first draft of the manuscript. I. S. B. and L. C. fabricated and tested the large area printed PSCs under the supervision of D. B. E. J. Y. performed DFT calculations on fullerene dimers and trimers and validated other DFT results. M. R. performed and analysed the HPLC under the supervision of M. H. and N. G. H. D. prepared the neat and blend C_{60} and C_{60}:BCP films under the supervision of S. H. Y. C. C. and T. L. assisted with the validation and interpretation of APS, Kelvin probe and SPV data. J. S. K conceived the study and supervised the whole project, directed/revised the manuscript, and procured funding. All authors contributed to the discussion of results and final version of the manuscript.

Conflicts of interest

There are no conflicts to declare.

Acknowledgements

C. H. acknowledges the UK EPSRC for DTP studentship and Oninn for CASE studentship support. This research was supported by the EPSRC ATIP Programme Grant (EP/T028513/1). I. S. B, C. L. and D. B. acknowledge CEMIG (Companhia Energética de Minas Gerais S. A.) for financial support (04951-0660/2022 – ANEEL). The authors thank Chiara Labanti for her assistance with sample fabrication.

References

1 J. Park, J. Kim, H.-S. Yun, M. J. Paik, E. Noh, H. J. Mun, M. G. Kim, T. J. Shin and S. Il Seok, *Nature*, 2023, **616**, 724–730.
2 L. Lin, L. Yang, G. Du, X. Li, Y. Li, J. Deng, K. Wei and J. Zhang, *ACS Appl. Energy Mater.*, 2023, **6**, DOI: **10.1021/acsaem.2c04120**.
3 S. Shao and M. A. Loi, *Adv. Mater. Interfaces*, 2020, **7**, 1901469.
4 C. Zhao, B. Chen, X. Qiao, L. Luan, K. Lu and B. Hu, *Adv. Energy Mater.*, 2015, **5**, 1500279.
5 J. Hu, R. Gottesman, L. Gouda, A. Kama, M. Priel, S. Tirosh, J. Bisquert and A. Zaban, *ACS Energy Lett.*, 2017, **2**, 950–956.
6 S. Shao, M. Abdu-Aguye, L. Qiu, L.-H. Lai, J. Liu, S. Adjokatse, F. Jahani, M. E. Kamminga, G. H. ten Brink, T. T. M. Palstra, B. J. Kooi, J. C. Hummelen and M. Antonietta Loi, *Energy Environ. Sci.*, 2016, **9**, 2444–2452.
7 J. Luke, L. Corrêa, J. Rodrigues, J. Martins, M. Daboczi, D. Bagnis and J. Kim, *Adv. Energy Mater.*, 2021, **11**, 2003405.
8 M. M. Lee, J. Teuscher, T. Miyasaka, T. N. Murakami and H. J. Snaith, *Science*, 2012, **338**, 643–647.
9 X. Lin, D. Cui, X. Luo, C. Zhang, Q. Han, Y. Wang and L. Han, *Energy Environ. Sci.*, 2020, **13**, 3823–3847.
10 S. Zhang, F. Ye, X. Wang, R. Chen, H. Zhang, L. Zhan, X. Jiang, Y. Li, X. Ji, S. Liu, M. Yu, F. Yu, Y. Zhang, R. Wu, Z. Liu, Z. Ning, D. Neher, L. Han, Y. Lin, H. Tian, W. Chen, M. Stolterfoht, L. Zhang, W. Zhu and Y. Wu, *Science*, 2023, **380**, 404–409.
11 Q. Tan, Z. Li, G. Luo, X. Zhang, B. Che, G. Chen, H. Gao, D. He, G. Ma, J. Wang, J. Xiu, H. Yi, T. Chen and Z. He, *Nature*, 2023, 32–34.

12 H. Gommans, B. Verreet, B. P. Rand, R. Muller, J. Poortmans, P. Heremans and J. Genoe, *Adv. Funct. Mater.*, 2008, **18**, 3686–3691.
13 R. Tomova, P. Petrova and R. Stoycheva-Topalova, *Phys. Status Solidi C*, 2010, **7**, 992–995.
14 Y. Bai, X. Meng and S. Yang, *Adv. Energy Mater.*, 2018, **8**, 1701883.
15 H. Yoshida, *J. Phys. Chem. C*, 2015, **119**, 24459–24464.
16 Y. Nakayama, T. L. Nguyen, Y. Ozawa, S. Machida, T. Sato, H. Tokairin, Y. Noguchi and H. Ishii, *Adv. Energy Mater.*, 2014, **4**, 1301354.
17 C. Chen, S. Zhang, S. Wu, W. Zhang, H. Zhu, Z. Xiong, Y. Zhang and W. Chen, *RSC Adv.*, 2017, **7**, 35819–35826.
18 M. Vogel, S. Doka, C. Breyer, M. C. Lux-Steiner and K. Fostiropoulos, *Appl. Phys. Lett.*, 2006, **89**, 163501.
19 B. R. Patil, M. Ahmadpour, G. Sherafatipour, T. Qamar, A. F. Fernández, K. Zojer, H.-G. Rubahn and M. Madsen, *Sci. Rep.*, 2018, **8**, 12608.
20 J. Lee, S. Park, Y. Lee, H. Kim, D. Shin, J. Jeong, K. Jeong, S. W. Cho, H. Lee and Y. Yi, *Phys. Chem. Chem. Phys.*, 2016, **18**, 5444–5452.
21 G. H. Jung and J.-L. Lee, *J. Mater. Chem. A*, 2013, **1**, 3034.
22 H. Lee, G. Cho, S. Woo, S. Nam, J. Jeong, H. Kim and Y. Kim, *RSC Adv.*, 2012, **2**, 8762.
23 D. Burkitt, R. Patidar, P. Greenwood, K. Hooper, J. McGettrick, S. Dimitrov, M. Colombo, V. Stoichkov, D. Richards, D. Beynon, M. Davies and T. Watson, *Sustainable Energy Fuels*, 2020, **4**, 3340–3351.
24 D.-K. Lee and N.-G. Park, *Sol. RRL*, 2022, **6**, 2100455.
25 Y. Wang, C. Duan, P. Lv, Z. Ku, J. Lu, F. Huang and Y.-B. Cheng, *Natl. Sci. Rev.*, 2021, **8**, DOI: 10.1093/nsr/nwab075.
26 S. Castro-Hermosa, L. Wouk, I. S. Bicalho, L. de Queiroz Corrêa, B. de Jong, L. Cinà, T. M. Brown and D. Bagnis, *Nano Res.*, 2021, **14**, 1034–1042.
27 M. Daboczi, I. Hamilton, S. Xu, J. Luke, S. Limbu, J. Lee, M. A. McLachlan, K. Lee, J. R. Durrant, I. D. Baikie and J.-S. Kim, *ACS Appl. Mater. Interfaces*, 2019, **11**, 46808–46817.
28 L. Kronik and Y. Shapira, *Surf. Interface Anal.*, 2001, **31**, 954–965.
29 M. Daboczi, J. Kim, J. Lee, H. Kang, I. Hamilton, C. Lin, S. D. Dimitrov, M. A. McLachlan, K. Lee, J. R. Durrant and J. Kim, *Adv. Funct. Mater.*, 2020, **30**, 2001482.
30 M. Daboczi, S. R. Ratnasingham, L. Mohan, C. Pu, I. Hamilton, Y.-C. Chin, M. A. McLachlan and J.-S. Kim, *ACS Energy Lett.*, 2021, **6**, 3970–3981.
31 Y.-C. Chin, M. Daboczi, C. Henderson, J. Luke and J.-S. Kim, *ACS Energy Lett.*, 2022, **7**, 560–568.
32 F. Zu, C. M. Wolff, M. Ralaiarisoa, P. Amsalem, D. Neher and N. Koch, *ACS Appl. Mater. Interfaces*, 2019, **11**, 21578–21583.
33 N. Aristidou, I. Sanchez-Molina, T. Chotchuangchutchaval, M. Brown, L. Martinez, T. Rath and S. A. Haque, *Angew. Chem., Int. Ed.*, 2015, **54**, 8208–8212.
34 M. Sakomura, Y. Yokokura, Y. Takagi and K. Ueda, *AIP Adv.*, 2020, **10**, 015144.
35 P.-W. Liang, C.-C. Chueh, S. T. Williams and A. K.-Y. Jen, *Adv. Energy Mater.*, 2015, **5**, 1402321.
36 A. Dzwilewski, T. Wågberg and L. Edman, *J. Am. Chem. Soc.*, 2009, **131**, 4006–4011.
37 Z. Li, H. C. Wong, Z. Huang, H. Zhong, C. H. Tan, W. C. Tsoi, J. S. Kim, J. R. Durrant and J. T. Cabral, *Nat. Commun.*, 2013, **4**, 2227.
38 D. S. Bethune, G. Meijer, W. C. Tang and H. J. Rosen, *Chem. Phys. Lett.*, 1990, **174**, 219–222.
39 T. J. Dennis, J. P. Hare, H. W. Kroto, R. Taylor, D. R. M. Walton and P. J. Hendra, *Spectrochim. Acta, Part A*, 1991, **47**, 1289–1292.
40 A. Distler, T. Sauermann, H.-J. Egelhaaf, S. Rodman, D. Waller, K.-S. Cheon, M. Lee and D. M. Guldi, *Adv. Energy Mater.*, 2014, **4**, 1300693.
41 S. Pont, J. R. Durrant and J. T. Cabral, *Adv. Energy Mater.*, 2019, **9**, 1803948.
42 T. Heumueller, W. R. Mateker, A. Distler, U. F. Fritze, R. Cheacharoen, W. H. Nguyen, M. Biele, M. Salvador, M. von Delius, H.-J. Egelhaaf, M. D. McGehee and C. J. Brabec, *Energy Environ. Sci.*, 2016, **9**, 247–256.
43 P. Hang, J. Xie, C. Kan, B. Li, Y. Zhang, P. Gao, D. Yang and X. Yu, *Adv. Mater.*, 2021, **33**, 2006910.
44 Y. Wang, J. M. Holden, Z.-H. Dong, X.-X. Bi and P. C. Eklund, *Chem. Phys. Lett.*, 1993, **211**, 341–345.
45 A. M. Rao, P. Zhou, K.-A. Wang, G. T. Hager, J. M. Holden, Y. Wang, W.-T. Lee, X.-X. Bi, P. C. Eklund, D. S. Cornett, M. A. Duncan and I. J. Amster, *Science*, 1993, **259**, 955–957.
46 S. Lebedkin, A. Gromov, S. Giesa, R. Gleiter, B. Renker, H. Rietschel and W. Krätschmer, *Chem. Phys. Lett.*, 1998, **285**, 210–215.
47 H. Chadli, A. Rahmani and J.-L. Sauvajol, *J. Phys.: Condens. Matter*, 2010, **22**, 145303.
48 P. A. Forero Cortés, M. Marx, M. Trose and M. Beller, *Chem Catal.*, 2021, **1**, 298–338.
49 D. Wang, A. B. Weinstein, P. B. White and S. S. Stahl, *Chem. Rev.*, 2018, **118**, 2636–2679.
50 T. Liu, L. Sun, C. Xie, W. Wang, F. Qin and Y. Zhou, *J. Mater. Chem. A*, 2021, **9**, 23269–23275.
51 S. Wood, J. Wade, M. Shahid, E. Collado-Fregoso, D. D. C. Bradley, J. R. Durrant, M. Heeney and J.-S. Kim, *Energy Environ. Sci.*, 2015, **8**, 3222–3232.
52 S. Pont, S. Osella, A. Smith, A. V. Marsh, Z. Li, D. Beljonne, J. T. Cabral and J. R. Durrant, *Chem. Mater.*, 2019, **31**, 6076–6083.
53 J. Warby, F. Zu, S. Zeiske, E. Gutierrez-Partida, L. Frohloff, S. Kahmann, K. Frohna, E. Mosconi, E. Radicchi, F. Lang, S. Shah, F. Peña-Camargo, H. Hempel, T. Unold, N. Koch, A. Armin, F. De Angelis, S. D. Stranks, D. Neher and M. Stolterfoht, *Adv. Energy Mater.*, 2022, **12**, 2103567.
54 J. Wu, J. Lee, Y.-C. Chin, H. Yao, H. Cha, J. Luke, J. Hou, J.-S. Kim and J. R. Durrant, *Energy Environ. Sci.*, 2020, **13**, 2422–2430.
55 C. Labanti, J. Wu, J. Shin, S. Limbu, S. Yun, F. Fang, S. Y. Park, C. Heo, Y. Lim, T. Choi, H.-J. Kim, H. Hong, B. Choi, K. Park, J. R. Durrant and J. Kim, *Nat. Commun.*, 2022, **13**, 3745.
56 Y. Fu, T. H. Lee, Y.-C. Chin, R. A. Pacalaj, C. Labanti, S. Y. Park, Y. Dong, H. W. Cho, J. Y. Kim, D. Minami, J. R. Durrant and J.-S. Kim, *Nat. Commun.*, 2023, **14**, 1870.

57 J. Marin-Beloqui, G. Zhang, J. Guo, J. Shaikh, T. Wohrer, S. M. Hosseini, B. Sun, J. Shipp, A. J. Auty, D. Chekulaev, J. Ye, Y.-C. Chin, M. B. Sullivan, A. J. Mozer, J.-S. Kim, S. Shoaee and T. M. Clarke, *J. Phys. Chem. C*, 2022, **126**, 2708–2719.
58 S. Lee, D. Bin Kim, I. Hamilton, M. Daboczi, Y. S. Nam, B. R. Lee, B. Zhao, C. H. Jang, R. H. Friend, J.-S. Kim and M. H. Song, *Adv. Sci.*, 2018, **5**, 1801350.
59 D. Wang, T. Ye and Y. Zhang, *J. Mater. Chem. A*, 2020, **8**, 20819–20848.
60 I. D. Baikie and P. J. Estrup, *Rev. Sci. Instrum.*, 1998, **69**, 3902–3907.
61 I. D. Baikie, A. Grain, J. Sutherland and J. Law, *Phys. Status Solidi C*, 2015, **12**, 259–262.
62 M. L. Laury, M. J. Carlson and A. K. Wilson, *J. Comput. Chem.*, 2012, **33**, 2380–2387.